# Modeling the Ice-Age Climate

## The July climate of 18,000 years ago has been simulated with a global atmospheric model.

W. Lawrence Gates

The last great (Wisconsin) ice age has long held the interest of climatologists, geologists, and geographers as the best documented of the several ice ages of the last million years. Although local glaciation maximums varied by several thousand years, the time 18,000 B.P. (years before present) is globally representative of this event. The changes of flora and fauna that accompanied this ice age are recorded in an extensive paleoclimatic literature, and are supplemented by widespread evidence of changes in the physical character of the earth's surface, such as changes in sea level, sea-ice extent, and local orography. From these and other evidence, estimates of the local nature of the ice-age climate itself have been derived at selected sites in terms of such variables as the local wind, temperature, or rainfall. Although they are insufficient to portray the overall global climatic regime, these estimates indicate that the ice-age climate was substantially different from today's in many regions of the world.

The purpose of this article is to report the initial results of a simulation of ice-age climate with a global atmospheric model and to make a preliminary comparison of these results with available paleoclimatic evidence. Although such a model simulates only the atmosphere's response to the prescribed distributions of sea-surface temperature, ice, and snow, it constitutes a useful first step in the systematic investigation of the structure of paleoclimates. When such global climatic syntheses have been achieved at a number of time levels, it may be possible to apply more complete models in which the oceans, sea ice, snow cover, and ice sheets, as well as the atmosphere, are treated as time-dependent parts of the climatic system. Only then can the many questions of ice-age climatic change be addressed.

In order to lay a firmer observational basis for the study of ice-age climates, the CLIMAP project has recently undertaken the systematic assembly of global paleoclimatic data at the time 18,000 B.P. (*1*). As a result of these efforts, the first estimates of the worldwide distribution of July sea-surface temperatures have now been produced from the statistical analysis of the distribution of temperature-sensitive marine microorganisms found at the appropriate levels in dated deep-sea cores (*2*). CLIMAP has also assembled new data on the global distribution and thickness of the 18,000 B.P. ice sheets and major mountain glacier systems, and on the distribution of the albedo of the 18,000 B.P. land, snow-, and ice-covered surfaces (*1*).

These data are precisely those required for global models of the general atmospheric circulation, and were assembled by CLIMAP in anticipation of their use for the model described below. This model is capable of simulating in a dynamically consistent fashion the global distribution of the various climatic elements (such as pressure, temperature, wind, cloudiness, and precipitation) that are in equilibrium with the specified ice-age boundary conditions. Such a climatic reconstruction may then be "verified" by data that were not used in the model calculations—for example, land-based estimates of paleoclimatic temperature. An extended analysis of the atmospheric simulation will be presented elsewhere (*3*).

### Paleoclimatic and Present Surface Conditions

The global distributions of the surface conditions for July and August 18,000 B.P. as reconstructed by CLIMAP are shown in Fig. 1. The sea-surface temperature analysis is based on data interpolated onto a global grid 4° in latitude by 5° in longitude from several hundred deep-sea cores (*1, 2*). Also given in Fig. 1 are the extent of continental ice sheets, major mountain glacier systems (including snow-covered land), and sea ice as reconstructed by CLIMAP on the grid; the continental outlines are those corresponding to a sea-level lowering of 85 m (with respect to present). Sea ice was assigned to all ocean points poleward of the analyzed −1.5°C isotherm that were not covered by grounded ice sheets.

The elevation of all ice-covered surfaces was also estimated by CLIMAP (*1*), and was combined with the elevation of surfaces that are ice-free at present to form a global ice-age topography with respect to ice-age sea level. The maximum elevations (with respect to sea level) are 2900 m near 58N,90W (Laurentide), 3580 m near 74N,40W (Greenland), 3080 m near 62N,20E (Scandinavian), 2880 m near 66N,100E (Siberian), and 2580 m near 54S,70W (Argentine). The Antarctic ice sheet's maximum elevation was estimated as 4040 m near 82S,75E. The thickness of a number of extensive mountain glacier systems was also considered at scattered locations (see Fig. 1). The albedo estimated by CLIMAP for ice-covered surfaces has maximums of 0.90 over portions of Antarctica (0.80 over parts of the other major ice sheets) and 0.80 and 0.70 over Antarctic and Arctic sea ice, respectively. Partially glaciated or snow-covered surfaces were assigned albedos ranging downward from these values to 0.40. The albedo of bare land surfaces was generally within the range 0.14 to 0.28, with a maximum of 0.30 over deserts such as the Sahara (*1*). The albedo of all ice-age ocean points was taken as at present (between 0.06 and 0.09, depending on latitude). Details of the surface elevation and albedo are given elsewhere (*3*).

The global distributions of the surface conditions for present July are shown in Fig. 2 in a format similar to that of Fig. 1. The sea-surface temperature and sea ice limits, and the present land and ice surface elevations (not shown), have been derived from new global tabulations (*4*). The maximum elevations of the present Greenland and Antarctic ice sheets are taken as 2380 m near 74N,40W and 3450 m near 82S,90E, respectively. The surface albedo of ice-free land areas for present July conditions was interpolated onto the grid from available seasonally averaged data (*5*); values of 0.80 and 0.70 were assigned to the Antarctic ice sheet and surrounding sea ice, respectively, 0.75 to the Greenland ice sheet, and 0.50 to Arctic sea ice. A maximum bare-land albedo of 0.30 was assigned in the desert regions of North Africa, the Middle East, and Australia.

A summary of the July ice-age and

The author is director of the Climate Dynamics Program at the Rand Corporation, Santa Monica, California 90406, and is a cooperating member of CLIMAP.

present surface conditions is given in Table 1. The area-weighted surface albedo for the ice age in both hemispheres is 57 percent greater than the present global value of 0.14. This is due to the substantial increase in the extent of the continental ice sheets, especially in the Northern Hemisphere, and to the greatly increased sea ice in the Southern Hemisphere (*6*). These data indicate that 18.2 percent of the ice-age earth was ice-covered, nearly double the present value of 9.3 percent. When the sea-surface temperature is averaged over the respective ice-free portions of the ice-age and present oceans, the surface of the ice-age oceans is only 0.9°C colder, on the average, than the present July sea surface. However, the globally averaged difference between the ice-age and present sea-surface temperatures (found from the open-water points common to both the ice-age and present geographies) is −2.3°C. The largest local anomalies of sea-surface temperature (ice age minus present) occur in the North Atlantic poleward of about 40N (where the maximum change is −17.2°C near 42N,60W and in the eastern equatorial Pacific (where the maximum change is −7.1°C near 6S,150W). The sea-surface temperature is actually higher in the ice age than at present at a number of locations, including the subtropical portions of the eastern North Pacific and eastern North Atlantic, and the western portion of the central North Pacific (where the maximum change is +3.3°C near 46N,165E).

## Atmospheric Model

These boundary conditions have been used with an atmospheric model that represents the global tropospheric circulation in terms of the mathematical equations governing large-scale atmospheric motion; these are the equations of (horizontal) motion, the thermodynamic energy equation, the hydrostatic equation, and continuity equations for atmospheric mass and water vapor. When written in terms of two tropospheric layers of equal mass between the (variable) surface pressure ($p_s$) and the assigned upper boundary surface at 200 mbar, as illustrated in Fig. 3, such a model permits the determination of the time-dependent behavior of the temperature ($T$) and horizontal velocity ($\vec{V}$) at two levels approximating the 400-mbar and 800-mbar surfaces (*7*). In the version of the model used, the water vapor mixing ratio ($q$) is also predicted at the lower level, along with the surface evaporation ($E$) and the cloudiness and precipitation ($P$) resulting from both large-scale vertical motion (determined midway between the upper and lower levels) and smaller-scale vertical convection (invoked to avoid unstable vertical stratification).

The model is thermodynamically driven by the diabatic heating due to the absorption of both long- and shortwave radiation, the latent heat released by condensation, and the vertical (turbulent) flux of sensible heat from the surface; each of these is parameterized in the model in terms of the large-scale distributions of temperature, pressure, velocity, and moisture, including the effects of clouds. At the surface, the elements of the heat and hydrologic balances are also simulated, along with the effects of surface friction. Upon prescription of the sea-surface temperature, surface elevation, surface albedo,

Table 1. Summary of area-averaged surface boundary conditions for ice-age (18,000 B.P.) and present July.

| Variable | Ice-age average | | Present average | |
|---|---|---|---|---|
| | Northern Hemisphere | Southern Hemisphere | Northern Hemisphere | Southern Hemisphere |
| Surface albedo | 0.20 | 0.24 | 0.12 | 0.16 |
| Sea-surface temperature* (°C) | 22.2 | 15.8 | 23.0 | 16.9 |
| Ice-free water area† ($10^6$ km$^2$) | 129.1 | 166.0 | 142.7 | 186.5 |
| Sea-ice area ($10^6$ km$^2$) | 9.7 | 34.5 | 10.4 | 19.8 |
| Ice sheet area‡ ($10^6$ km$^2$) | 31.7 | 17.2 | 4.3 | 13.1 |
| Bare land area ($10^6$ km$^2$) | 84.5 | 37.3 | 97.6 | 35.6 |

*Averaged over ice-free ocean areas in each case. †Including ice-free lakes. ‡Including snow-covered land.

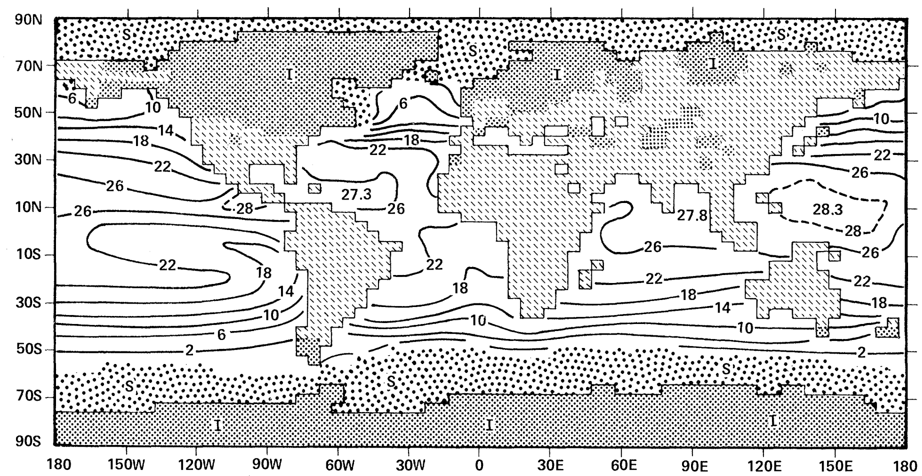


Fig. 1. Ice-age (18,000 B.P.) surface boundary conditions as assembled by CLIMAP for July and August (*1*). The sea-surface temperature is in degrees Celsius and the ice-age land outline is that resolved on a global grid 4° in latitude by 5° in longitude. The symbols *S* and *I* within the shaded areas denote the assigned locations of sea ice and ice sheets (including snow-covered land), respectively.

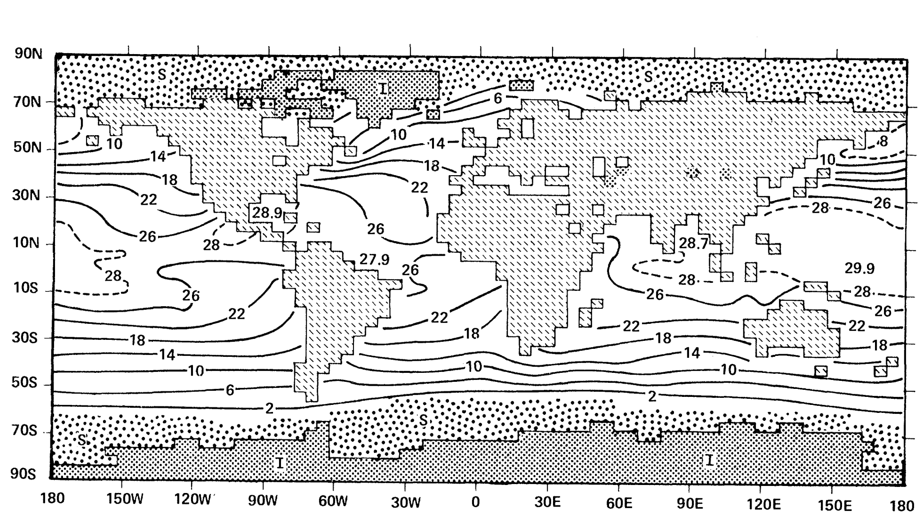


Fig. 2. Present July surface boundary conditions as assembled from modern data (*4, 5*). Symbols and units are as in Fig. 1.

and surface character (that is, whether bare land or ice-covered), the model calculates all of the time-dependent atmospheric variables, including the ground temperature over land and ice-covered surfaces in response to diurnally and seasonally varying solar radiation. Details of these and other model calculations are given elsewhere (*8*).

When the model's equations are written in suitable finite-difference form on a grid network covering the spherical earth (and with due provisions made for computational stability), solutions for the complete set of modeled variables over the globe may be computed as a function of time by stepwise numerical integration. With a global grid of 4° in latitude and 5° in longitude, the model's integration proceeds in simulated time steps of 6 minutes, with the heating, friction, and moisture source terms computed every 30 minutes. Execution of the program on an IBM 360-91 requires about 15 minutes of computer time to simulate 1 day. Starting from realistic initial conditions appropriate to 1 May (previously generated by the model with present boundary conditions), the numerical solutions were carried out for 92 days corresponding to the months of May, June, and July with the fixed ice-age boundary conditions described above (see Fig. 1); the ice-age July climate was then determined by time-averaging the solutions over the last 31 days of the integration.

When applied in a similar fashion with the present July surface boundary conditions shown in Fig. 2, the model successfully simulates the major features of the observed July distributions of pressure, temperature, and circulation (*9*). As shown in Fig. 4, the simulated July sea-level pressure map portrays the observed high-pressure cells over the North Atlantic and northeast North Pacific oceans, along with the observed low-pressure centers over eastern Canada, near the British Isles, and over southeast Asia. In the Southern Hemisphere the observed subtropical belt of high pressure near 30S is also present, although the highest pressure is generally simulated farther to the east (and somewhat more over the southern continents) than the observed high-pressure centers in July. The low pressure surrounding Antarctica is also successfully simulated, although this feature's observed structure is not well established.

The major shortcomings of the model's July simulation occur in the distribution of cloudiness and precipitation. The model systematically simulates more total precipitation than is observed, especially in the lower latitudes (where its simulation is nearly double the observed precipitation). This error appears to be associated with the model's portrayal of excessive deep convective activity in the tropics, and produces an average temperature at 400 mbar nearly 10°C above that observed in the region between 30N and 30S (*9*). The simulated total July cloudiness is systematically lower than that observed over most of the Northern Hemisphere, and the simulated average July cloudiness of about 0.3 is far below the value 0.8 observed over the Arctic basin. This error is thought to be related to the present model's neglect of the presence of nonprecipitating clouds, especially of the stratus type, and to its neglect of moisture at the upper model level. In spite of these deficiencies, the surface balance of heat (measuring the combined effects of absorbed long- and shortwave radiation and the surface fluxes of latent and sensible heat) and the surface balance of moisture (as measured by the evaporation-precipitation difference) are simulated with reasonable accuracy. This lends credence to the hypothesis that at least the differences in the model's simulations for the ice-age and present July climates are realistic (*3*).

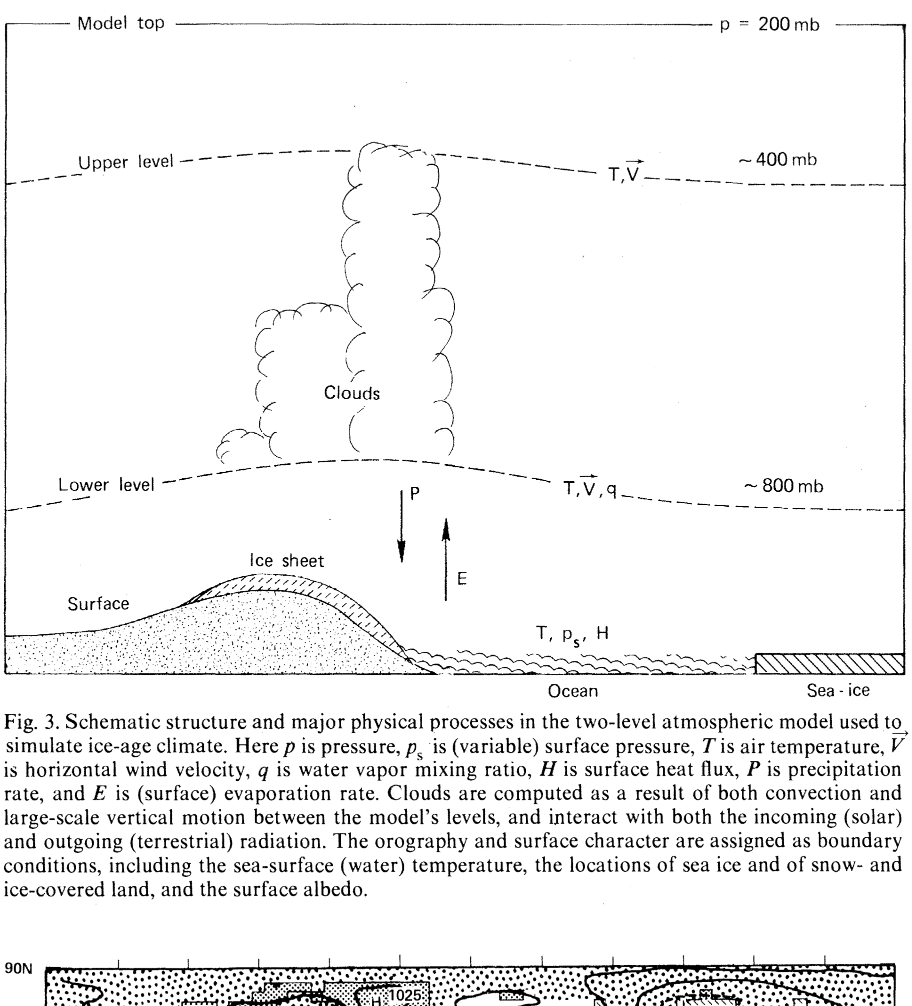


Fig. 3. Schematic structure and major physical processes in the two-level atmospheric model used to simulate ice-age climate. Here $p$ is pressure, $p_s$ is (variable) surface pressure, $T$ is air temperature, $\vec{V}$ is horizontal wind velocity, $q$ is water vapor mixing ratio, $H$ is surface heat flux, $P$ is precipitation rate, and $E$ is (surface) evaporation rate. Clouds are computed as a result of both convection and large-scale vertical motion between the model's levels, and interact with both the incoming (solar) and outgoing (terrestrial) radiation. The orography and surface character are assigned as boundary conditions, including the sea-surface (water) temperature, the locations of sea ice and of snow- and ice-covered land, and the surface albedo.

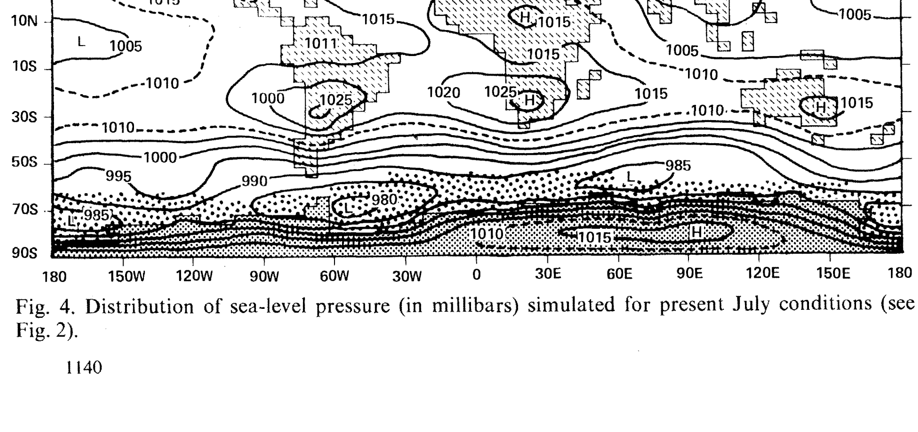


Fig. 4. Distribution of sea-level pressure (in millibars) simulated for present July conditions (see Fig. 2).

### Simulated Ice-Age Climate

The distribution of July sea-level pressures simulated for the ice-age boundary conditions of Fig. 1 is shown in Fig. 5. Prominent high-pressure regions are simulated over the major ice sheets in the Northern Hemisphere, indicating a strengthened surface air flow from the east and northeast in central Europe, Siberia, and central North America in the regions immediately south of the ice sheets. Over the eastern United States and Canada and over western Europe this is in sharp contrast to the generally southerly and southwesterly flow inferred from the results for present July conditions (see Fig. 4). At the same time the anticyclones simulated over the North Atlantic and North Pacific oceans under present conditions (Fig. 4) are only slightly changed in the ice-age case (Fig. 5), and the North American low-pressure trough has shifted to a position off the east coast of the ice-age continent. The Asian low-pressure system corresponding to that off the east coast of North America is displaced inland in the ice age relative to its present position near southern Japan, while the low-pressure area associated with the summer Asiatic monsoon near India has remained essentially intact. The ice-age sea-level pressure pattern in the lower latitudes of both hemispheres is little changed from that of today, while the ice-age circumpolar low-pressure pattern in high southern latitudes is slightly weaker than at present and is found near the northern edge of the sea ice. These changes may also be seen in the zonally averaged sea-level pressure shown in Fig. 6, in which the ice-age sea-level pressure has been normalized to yield the same total sea-level pressure as at present (*10*).

Perhaps of greater climatic interest (and offering more possibility of verification) are the simulated differences in the surface air temperature for the ice-age and present July; these are shown in Fig. 7 at each land grid point that is ice-free in both present and ice-age July conditions (see Figs. 1 and 2). These data show a markedly lower ice-age surface air temperature over the regions of North America and Europe immediately to the south of the ice sheets, with cooling of as much as 10° to 15°C over extensive areas. Even greater cooling is simulated over portions of central Asia with extensive snow cover. Over South America, Africa, and Australia the simulated ice-age cooling averages about 5°C and exceeds the average cooling of the adjacent oceans imposed in Figs. 1 and 2. Aside from a number of scattered locations in Africa and Asia, the only region in which the July surface air temperature is simulated to have been higher in the ice age than at present occurs in western Siberia, to the east and south of the eastern lobe of the Scandinavian ice sheet. Here the simulated ice-age surface airflow is from the east (see Fig. 5), bringing air from the interior which is relatively warmer than that from the north off the ice-covered Arctic Ocean simulated for the present (see Fig. 4).

Also shown in Fig. 7 are the "observed" differences between present and ice-age surface air temperature at the sites for which such estimates are available; these data have been obtained from analyses of fossil pollen and other periglacial evidence (*11*). In most locations the agreement with the model's results is quite good, especially in view of the point-to-point variability exhibited by the simulated data. The largest disagreements occur in the East Indies, where the model's results are sensitive to inaccuracies in the simulated positions of the tropical rain belts, and in northwest Siberia, where the observed temperature changes disagree even in sign with those simulated. In these regions especially, additional verification is needed.

In locations that are now ice-free but were covered by ice sheets at 18,000 B.P., the ice-age surface air temperature is generally simulated to be much lower than at present; this is due both to the increased elevation and to the higher albedo of the ice cover. When all such locations are considered, including points at which sea ice is present at either one or both times, the surface air temperature varies in the zonal average as shown in Fig. 8. These data correspond to a globally averaged reduction of ice-age surface air temperature relative to the present of 4.9°C, in spite of the fact that the air temperature over the oceans remains close to the prescribed sea-surface temperature (see Table 1). At higher levels in the atmosphere the thermal effect of the surface is reduced, and the air temperature is more influenced by the large-scale atmospheric circulation. Figure 8 also shows the zonally averaged July temperature simulated at 400 mbar for both ice-age and

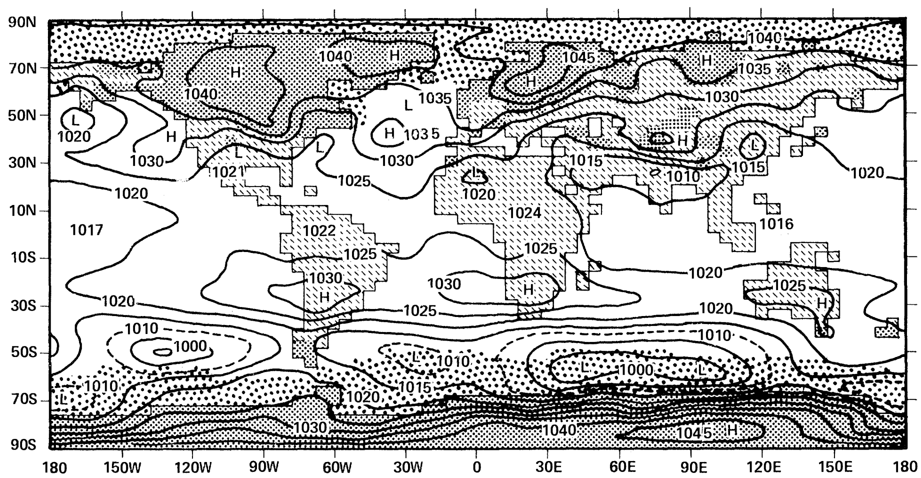


Fig. 5. Distribution of sea-level pressure (in millibars) simulated for ice-age (18,000 B.P.) July conditions (see Fig. 1), calculated with respect to the ice-age sea level (85 m lower than today's).

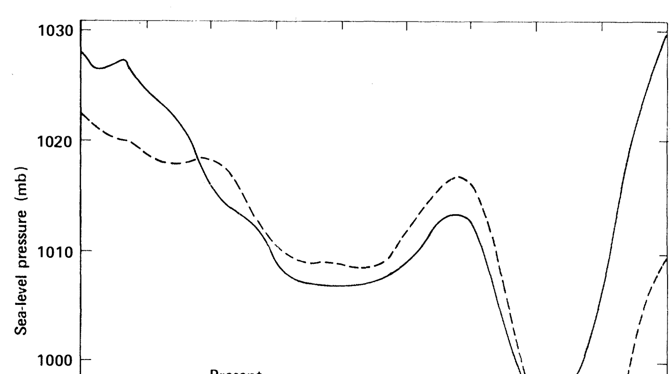


Fig. 6. Zonally averaged distribution of sea-level pressures for both ice-age and present July conditions. Here 12.7 mbar has been subtracted from the ice-age value at each latitude to facilitate comparison with today's case; see (*10*).

Table 2. Summary of area-averaged values of selected climatic variables for July ice-age conditions, and differences from present July simulations.

| Variable | Ice-age average | | Difference (ice age minus present) average | |
|---|---|---|---|---|
| | Northern Hemisphere | Southern Hemisphere | Northern Hemisphere | Southern Hemisphere |
| Ground temperature* (°C) | 17.8 | 7.6 | -5.3 | -4.5 |
| Surface air temperature (°C) | 18.0 | 7.1 | -5.3 | -4.5 |
| Temperature at 800 mbar (°C) | 7.8 | -3.3 | -5.0 | -4.6 |
| Temperature at 400 mbar (°C) | -23.4 | -30.7 | -8.2 | -5.0 |
| Zonal wind at 800 mbar (m $sec^{-1}$) | -0.9 | 3.6 | -0.3 | -0.9 |
| Zonal wind at 400 mbar (m $sec^{-1}$) | 2.4 | 14.7 | -0.1 | -2.1 |
| Cloudiness (%) | 22.5 | 44.2 | -2.9 | -2.2 |
| Relative humidity at 800 mbar (%) | 46.8 | 63.1 | -2.6 | +0.1 |
| Precipitable water (mm) | 14.2 | 12.9 | -8.3 | -3.9 |
| Evaporation (mm $day^{-1}$) | 4.0 | 3.5 | -0.5 | -0.9 |
| Precipitation (mm $day^{-1}$) | 4.5 | 3.1 | -1.2 | -0.1 |
| Surface pressure (mbar) | 972.9 | 995.1 | -8.7 | +8.7 |

*Includes assigned sea-surface temperature over oceanic areas.

present conditions; these data correspond to a globally averaged ice-age cooling at 6.6°C. This upward "amplification" of the surface cooling is apparently a result of the model's attempt to maintain a vertical temperature lapse rate close to that for saturated air in the equatorial and tropical regions (*12*).

Accompanying the ice-age temperature changes are a number of systematic changes in the large-scale tropospheric circulation, as illustrated in Fig. 9 for the July zonal wind at 400 mbar. The westerly wind maximum simulated near 60N under present conditions is shifted to near 40N and somewhat increased in strength in the ice age, with relatively weak flow replacing the present maximum near 60N. This southward shift and strengthening of the mean Northern Hemisphere westerlies in the ice age is a direct result of the southward displacement of the zone of maximum meridional (north-south) temperature gradient introduced by the expanded ice sheets. These changes in temperature gradient are clearly shown in the hemispheric temperature distributions, but may also be seen in a close inspection of Fig. 8. The equatorial easterlies are also increased at all levels, along with a slight strengthening of the westerlies in the Southern Hemisphere. Further analysis shows that the mean meridional circulation (a measure of the time-averaged mass flux in a north-south direction) is simulated to be about 30 percent weaker in the ice age than at present in the tropical regions where such circulation is predominant, although the positions of the most intense average rising and sinking motion continue to be found near 10N and 30S, respectively. The average sinking motion associated with the meridional circulation in both polar regions, on the other hand, is markedly strengthened and shifted equatorward in the ice-age case (*3*).

An area-averaged summary of the simulation of selected climatic variables for the ice-age July is given in Table 2, together with their differences with respect to the model's simulation of present July. Here ground temperature data consist of the assigned sea-surface temperature over oceanic areas and the temperature computed at the surface of both bare and ice-covered land through the assumption of a balance of the surface heat fluxes (*8*). This ground or surface temperature closely resembles the surface air temperature discussed earlier, but their difference controls in large measure the vertical flux of sensible heat. A net downward sensible heat flux is thus implied at the surface in the Northern Hemisphere, and a net upward flux in the Southern Hemisphere; this is confirmed in

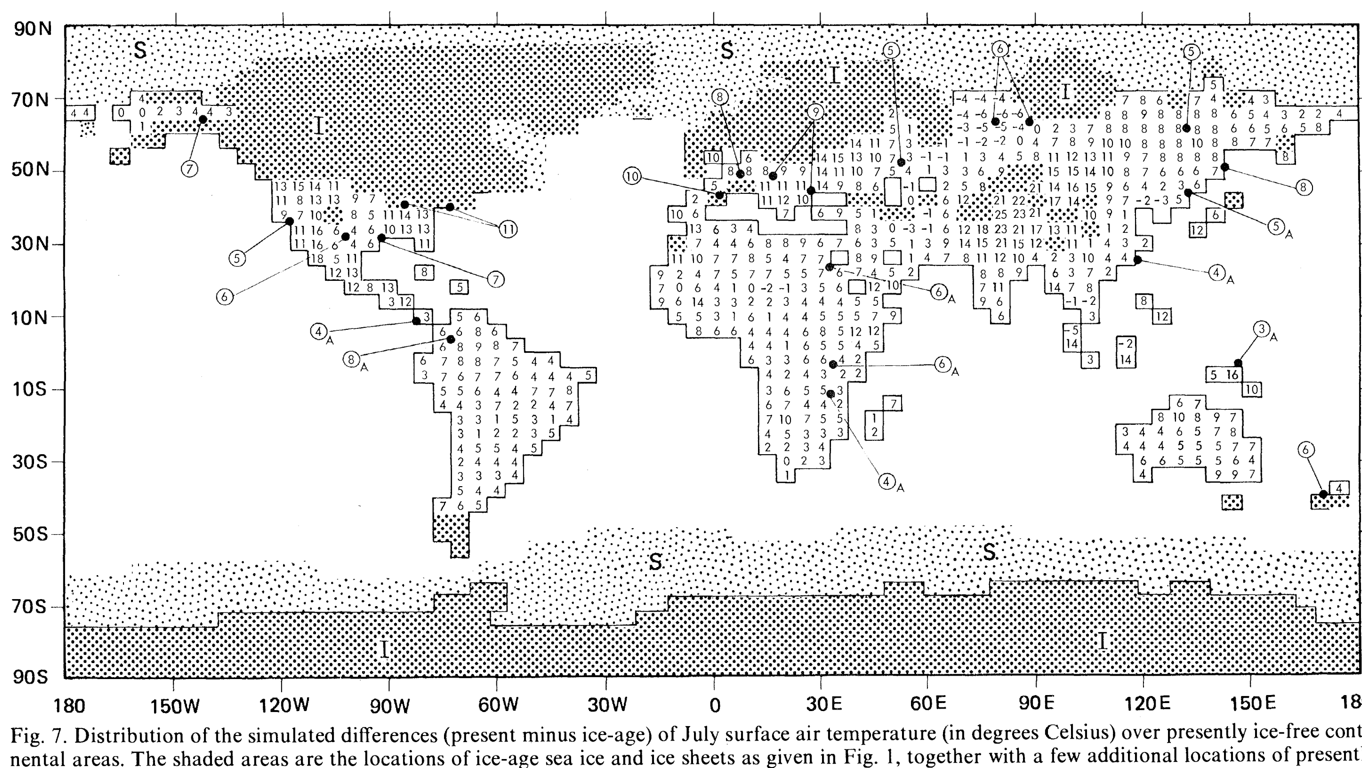


Fig. 7. Distribution of the simulated differences (present minus ice-age) of July surface air temperature (in degrees Celsius) over presently ice-free continental areas. The shaded areas are the locations of ice-age sea ice and ice sheets as given in Fig. 1, together with a few additional locations of presently snow-covered land from Fig. 2. The encircled data are the "observed" changes of surface air temperature as assembled by CLIMAP from pollen analyses and periglacial evidence; the encircled data with subscript A in the tropics are observed annual (rather than July) temperature changes.

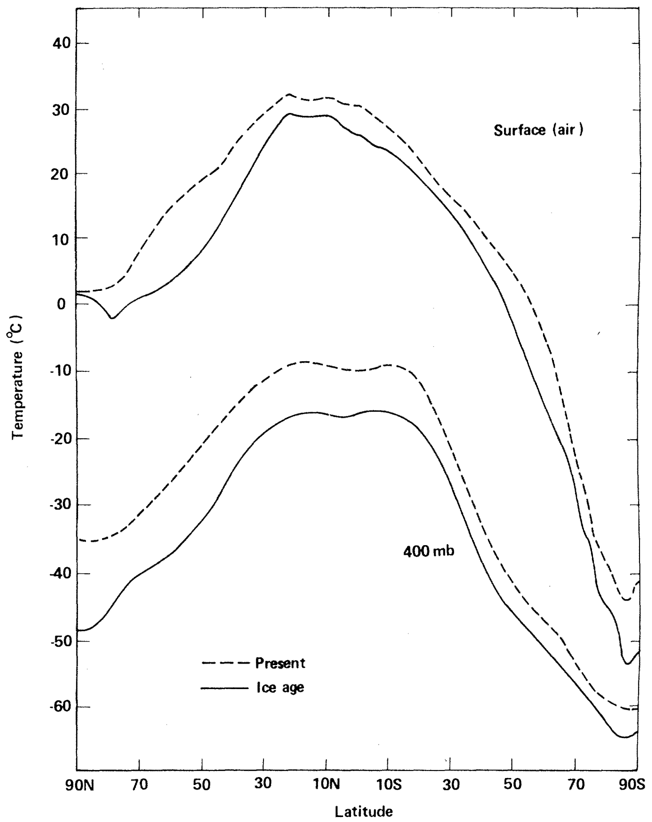


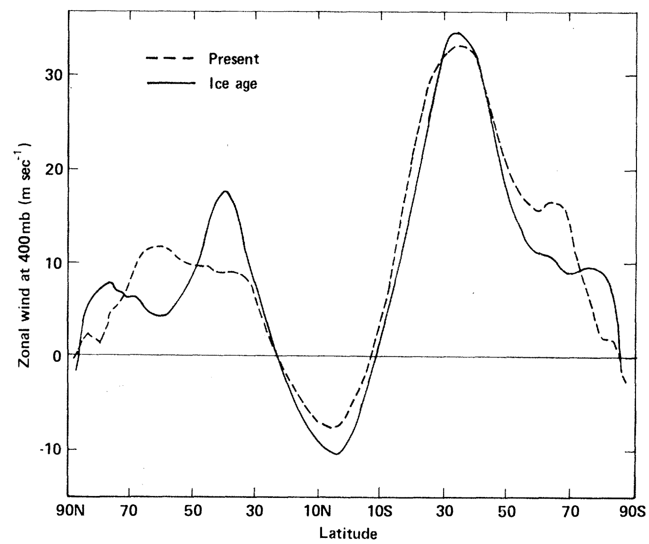


Fig. 8 (left). Zonally averaged distribution of surface air temperatures and 400-mbar temperatures for both ice-age and present July conditions. Fig. 9 (right). Zonally averaged distribution of zonal or westerly wind speeds for both ice-age and present July conditions.

a more complete analysis of the simulated heat budget (*3*).

Along with the global ice-age cooling and circulation shifts summarized here, there are small decreases in the total cloudiness and 800-mbar relative humidity, as shown in Table 2. The July ice-age atmosphere, however, contains somewhat less moisture than these data indicate, as the precipitable water (a measure of the total water vapor content in an air column) is decreased by about 37 and 23 percent of its present (simulated) July value in the Northern and Southern Hemisphere, respectively. The simulated ice-age evaporation and precipitation are also reduced by about 15 percent of their values simulated for the present July. The hemispheric averages of the differences between July evaporation and precipitation, moreover, indicate a net northward moisture transport between hemispheres during the ice-age corresponding to 0.4 mm/day, whereas the present transport is simulated to be three times larger. It is also of interest to note that the interhemispheric mass differential (as measured by the difference between the hemispheric averages of surface pressure) is simulated to be five times greater in the ice age than at present, due to both the displacement of air by the expanded Northern Hemisphere ice sheets and the worldwide lowering of sea level.

Although a more complete comparison of the present simulations of ice-age climate with the results given by others is presented elsewhere (*3*), it is of interest to at least indicate the degree of model dependence that may be present. In a previous simulation of ice-age July climate carried out at the National Center for Atmospheric Research (Boulder, Colorado) with a five-level atmospheric model (*13*), the simulated sea-level pressure distribution showed more drastic changes than those reported here. The high-pressure centers in the North Atlantic and eastern North Pacific oceans seen in Figs. 4 and 5 (and also simulated by the NCAR model for present July) were greatly smoothed and displaced northeastward and northwestward, respectively, while the monsoonal low-pressure system also prominent in Figs. 4 and 5 over southeast Asia and in the Middle East was virtually annihilated in the NCAR ice-age case. Generally cooler ice-age surface temperatures relative to those of the present were also found in the NCAR simulation (*14*), although a detailed comparison of simulated and "observed" surface air temperature changes, as in Fig. 7, was not made. In further contrast with the present results, the NCAR simulation gave no systematic southward displacement of the westerlies in the vicinity of the Northern Hemisphere ice sheets (as clearly shown in Fig. 9), and gave a precipitation reduction of about 50 percent over much of the Northern Hemisphere, together with an increase of cloudiness at nearly all latitudes. While it has not been established whether these differences in simulated ice-age climate are due to the differences in the surface boundary conditions used or to inherent differences in the models themselves, their existence reveals a high level of model-dependent sensitivity to boundary conditions, which needs to be further explored. Although additional simulations of the ice-age climate are necessary, other calculations using more simplified models (*15*) appear to support the overall validity of the present results, especially in terms of the simulated changes of the circulation pattern, temperature, and precipitation.

## Summary

Using the boundary conditions of sea-surface temperature, ice sheet topography, and surface albedo assembled by CLIMAP for 18,000 B.P., the global ice-age July climate has been simulated with a two-level dynamical atmospheric model. Compared with the simulation for present July climate, the ice age is substantially cooler and drier over the unglaciated continental areas, with the maximum zonal westerlies in the Northern Hemisphere displaced southward in the vicinity of the ice sheets. The simulated changes of surface air temperature agree reasonably well with the estimates available from the analysis of fossil pollen and periglacial data, and are consistent with the simulated changes of other climatic variables. These results are generally supported by independent investigations with simpler models.

In spite of this qualified success, further analysis of both simulated and verification data is needed to establish the details of ice-age climate, especially the precipitation regimes, and to document the role of eddy fluxes in maintaining the heat, momentum, and moisture balances of the ice-age general circulation. New paleoclimatic data bases for both July and January of 18,000 B.P. are being assembled by CLIMAP and will be used in new simulations of the seasonal ice-age climate.

### References and Notes


1. CLIMAP Project Members, *Science* **191**, 1131 (1976).
2. J. Imbrie and N. G. Kipp, in *The Late Cenozoic Glacial Ages*, K. Turekian, Ed. (Yale Univ. Press, New Haven, Conn., 1971), p. 71; A. McIntyre *et al., Geol. Soc. Am. Mem. 145*, in press.
3. W. L. Gates, *The Numerical Simulation of Ice-Age Climate with a Global General Circulation Model* (Rand Corporation, Santa Monica, Calif., in press).
4. W. L. Gates and A. B. Nelson, *A New Tabulation of the Scripps Topography on a 1° Global Grid*; Part I. *Terrain Heights* (R-1276, Rand Corporation, Santa Monica, Calif., 1973); R. C. Alexander and R. L. Mobley, *Monthly Average Sea-Surface Temperature and Ice-Pack Limits on a 1° Global Grid* (R-1310, Rand Corporation, Santa Monica, Calif., 1974).
5. J. W. Posey and P. F. Clapp, *Geofis. Int.* **4**, 33 (1964).
6. The small increase in the area of bare land in the ice age relative to the present in the Southern Hemisphere is due to the exposure of portions of the continental shelf by the 85-m lowering of sea level.
7. These levels are precisely defined in the model by $\sigma = 1/4$ and $\sigma = 3/4$ in terms of the vertical coordinate $\sigma = (p - 200 \text{ mbar})(p_S - 200 \text{ mbar})^{-1}$, where $p$ is pressure and $p_S$ is the (variable) surface pressure. In this coordinate system the earth's surface is always at $\sigma = 1$, and the presence of elevated terrain is automatically taken into account.
8. W. L. Gates, E. S. Batten, A. B. Kahle, A. B. Nelson, *A Documentation of the Mintz-Arakawa Two-Level Atmospheric General Circulation Model* (R-877, Rand Corporation, Santa Monica, Calif., 1971); W. L. Gates, *J. Atmos. Sci.* **32**, 449 (1975).
9. W. L. Gates and M. E. Schlesinger, "Numerical simulation of the January and July global climate with a two-level atmospheric model: a new comparison with observation" (unpublished manuscript, Rand Corporation, Santa Monica, Calif., 1975); C. Schutz and W. L. Gates, *Global Climatic Data for Surface, 800 mb, 400 mb: July* (R-1029, Rand Corporation, Santa Monica, Calif., 1972).
10. The globally averaged difference between the ice-age July sea-level pressure (Fig. 5) and present July sea-level pressure (Fig. 4) has been subtracted from the ice-age pressure at each latitude. This difference equals 12.7 mbar, and is principally due to the 85-m lowering of ice-age sea level; the total surface pressure (and hence the atmospheric mass) is conserved by the model in all cases.
11. These estimates have been assembled by T. Webb of Brown University from data published by B. Frenzel [*Climatic Fluctuations of the Ice Age* (Case Western Reserve University, Cleveland, 1973)] and from unpublished CLIMAP data.
12. E. B. Kraus, *Nature (London)* **245**, 129 (1973).
13. J. Williams, R. G. Barry, W. M. Washington, *J. Appl. Meteorol.* **13**, 305 (1974).
14. J. Williams, thesis, University of Colorado and National Center for Atmospheric Research, Boulder (1974); J. Williams and R. G. Barry, in *Climate of the Arctic*, G. Weller and S. A. Bowling, Eds. (University of Alaska, Fairbanks, 1975), p. 143.
15. F. N. Alyea, *Numerical Simulation of an Ice Age Paleoclimate* (Atmospheric Science Paper No. 193, Department of Atmospheric Science, Colorado State University, Ft. Collins, 1972); R. E. Newell and G. F. Herman, in *Proceedings of the WHO/IAMAP Symposium on Long-Term Climatic Fluctuations* (WMO 424, World Meteorological Organization, Geneva, 1975), p. 293; B. Saltzman and A. D. Vernekar, *Quat. Res.*, in press.


16. This research was supported by the Defense Advanced Research Projects Agency under contract DAHC15-73-C-0181 and by the National Science Foundation under grant ATM75-16923 AO1 and was conducted in cooperation with members of the CLIMAP project. I would like to thank T. Webb of Brown University for permitting me to use his compilations of observed ice-age temperature change and D. Pass for assistance in performing the model computations.


# Metal Ions in Enzymes Using Ammonia or Amides

A simple generalization provides fresh insights and makes specific predictions about some enzymes.


Nicholas E. Dixon, Carlo Gazzola, Robert L. Blakeley, Burt Zerner


The discovery that highly purified urease (E.C. 3.5.1.5) from jack beans (*Canavalia ensiformis*) contained stoichiometric amounts of nickel (*1*) developed out of two observations: (i) inhibition by two inhibitors of markedly disparate structure (acetohydroxamic acid and phosphoramidate) was slowly achieved and reversed (*2, 3*); and (ii) the enzyme showed a weak tail absorption extending from ~ 320 nm to a shoulder at ~ 425 nm, together with broad, weak maxima at 725 and 1060 nm (*1*).

In attempting to understand the role of nickel in the mechanism of action of urease, we have turned to other enzymes whose biological reactions involve ammonia as substrate, product, or as part of a transfer reaction. Many of these enzymes display apparently non-simple inhibition and activation effects, and, where the near-ultraviolet spectra are available, they are reminiscent of that of jack bean urease. In this article, we summarize evidence which suggests that various enzymes involved in reactions of ammonia may be partially understood in terms of two speculative postulates. (i) In every case there is a transition metal ion (or possibly an alkaline earth metal ion) more or less tightly bound to the enzyme; and (ii) the frequently postulated "enzyme-ammonia" intermediate in reactions catalyzed by these enzymes involves ammonia complexed to the bound metal ion.

An initial stumbling block in our thinking was the classical notion that the lack of an effect of ethylenediaminetetraacetate (EDTA) on an enzyme is substantial evidence for the absence of an essential metal ion. However, jack bean urease, with tightly bound active-site nickel ion (*1*), is at least the third example [together with yeast alcohol dehydrogenase (E.C. 1.1.1.1) and zinc ion (*4*), and chicken liver pyruvate carboxylase (E.C. 6.4.1.1) and manganous ion (*5*)] of an enzyme from which an active-site metal ion has thus far resisted all attempts at reversible removal (for example, by exhaustive dialysis in the presence of chelating agents or by exchange with a radioactive metal ion). Each of these enzymes is stable in the presence of EDTA at neutral $p$H, and in the case of urease, the enzyme is fully active in the presence of 0.5 m$M$ EDTA at neutral $p$H (*6*). These three examples establish firmly the proposition (*4*) that the absence of an effect of EDTA on an enzyme is not a sufficient basis on which to exclude the possibility of a tightly bound active-site transition metal ion. Fur-


Mr. Dixon and Mr. Gazzola are Commonwealth postgraduate students, Dr. Blakeley is a senior lecturer, and Dr. Zerner holds a personal Chair in the Department of Biochemistry, University of Queensland, St. Lucia, Queensland, Australia 4067.